Electron Reconnection in the Magnetopause Current Layer

C. Norgren, D B Graham, Yu V Khotyaintsev, M. André, A. Vaivads, M. Hesse, E Eriksson, P.-A Lindqvist, B. Lavraud, J. Burch, et al.

Journal of Geophysical Research: Space Physics

RESEARCH ARTICLE
10.1029/2018JA025676

Electron Reconnection in the Magnetopause Current Layer

C. Norgren[1,2], D. B. Graham[2], Yu. V. Khotyaintsev[2], M. André[2], A. Vaivads[2], M. Hesse[1], E. Eriksson[2,3], P.-A. Lindqvist[4], B. Lavraud[5], J. Burch[6], S. Fuselier[6,7], W. Magnes[8], D. J. Gershman[9,10], and C. T. Russell[11]

[1]Birkeland Centre for Space Science, Department of Physics and Technology, University of Bergen, Bergen, Norway, [2]Swedish Institute of Space Physics, Uppsala, Sweden, [3]Department of Physics and Astronomy, Uppsala University, Uppsala, Sweden, [4]Space and Plasma Physics, School of Electrical Engineering, KTH Royal Institute of Technology, Stockholm, Sweden, [5]Institut de Recherche en Astrophysique et Planétologie, CNRS, UPS, CNES, Université de Toulouse, Toulouse, France, [6]Southwest Research Institute, San Antonio, TX, USA, [7]Department of Physics and Astronomy, University of Texas at San Antonio, San Antonio, TX, USA, [8]Space Research Institute, Austrian Academy of Sciences, Graz, Austria, [9]Department of Astronomy, University of Maryland, College Park, MD, USA, [10]NASA Goddard Space Flight Center, Greenbelt, MD, USA, [11]Department of Earth and Space Sciences, University of California, Los Angeles, CA, USA

Key Points:
- A reconnecting electron scale current sheet is observed inside a filamented magnetopause current layer
- Due to a guide magnetic field and related magnetic curvature, electrons entering from opposite sides have different behavior
- The presence of an out-of-plane electric field can explain observed electron distributions

Correspondence to:
C. Norgren,
cecilia.norgren@uib.no

Citation:
Norgren, C., Graham, D. B., Khotyaintsev, Y. V., André, M., Vaivads, A., Hesse, M., et al. (2018). Electron reconnection in the magnetopause current layer. *Journal of Geophysical Research: Space Physics*, *123*, 9222–9238. https://doi.org/10.1029/2018JA025676

Received 21 MAY 2018
Accepted 9 OCT 2018
Accepted article online 18 OCT 2018
Published online 13 NOV 2018

Abstract The electron dynamics within thin current sheets plays a key role both for the process of magnetic reconnection and other energy transfer mechanisms but, from an observational point of view, is not well understood. In this paper we report observations of a reconnecting current sheet with intermediate guide field $B_G = 0.5B_{in}$, where B_{in} is the magnetic field amplitude in the inflow regions. The current sheet width is comparable to electron spatial scales. It shows a bifurcated structure and is embedded within the magnetopause current layer with thickness of several ion scales. The electron scale current sheet has strong out-of-plane and in-plane currents, Hall electric and magnetic fields, a finite magnetic field component normal to the current sheet, and nongyrotropic electron distributions formed due to finite gyroradius effects at the boundary of the current sheet. Comparison between test particle simulations and electron data shows that electrons approaching from the edge of the largest magnetic curvature are scattered to perpendicular pitch angles in the center of the current sheet while electrons entering from the opposite side remain close to field aligned. The comparison also shows that an observed depletion in phase space at antiparallel pitch angles can be explained if an out-of-plane electric field, which due to the guide field is close to antiparallel to the magnetic field, is present in the center of the current sheet. This electric field would be consistent with the reconnection electric field, and we therefore interpret the depletion of electron phase space density as a manifestation of ongoing reconnection.

1. Introduction

Magnetic reconnection (e.g., Biskamp, 2000; Priest & Forbes, 2000; Sonnerup, 1979, and references therein) is a fundamental plasma process in which the magnetic field topology changes and energy stored in the magnetic field is transferred to plasma particles, accelerating them. In near-Earth space, magnetic reconnection occurs both at large-scale boundaries such as the magnetopause (e.g., Mozer et al., 2002; Paschmann et al., 1979; Sonnerup et al., 1981; Vaivads et al., 2004) and in the magnetotail current sheet (e.g., Nagai et al., 2001; Wygant et al., 2005), and in more turbulent environments such as the solar wind (e.g., Gosling & Szabo, 2008) and the magnetosheath (e.g., Phan et al., 2018; Retinò et al., 2007; Sundkvist et al., 2007). Numerical simulations also suggest that magnetic reconnection can occur within the turbulent environment that can form downstream of the separatrices, where electron-scale filamentary current sheets can form (e.g., Daughton et al., 2011). Such filamentary currents have been observed inside a wider reconnection jet at the dayside magnetopause (Phan et al., 2016).

Magnetic reconnection is a multiscale process, where ions and electrons decouple from the magnetic field at ion and electron scales, respectively, and form the ion and electron diffusion regions (IDR and EDR). Inside the ion diffusion region, ion and electron motions differ, giving rise to currents and associated magnetic field structures (e.g. Sonnerup, 1979). These are referred to as Hall currents and magnetic fields and are commonly used to identify magnetic reconnection events (e.g., Eastwood et al., 2010; Nagai et al., 2001; Øieroset et al., 2001). Inside the electron diffusion region of width comparable to the electron inertial length, the electrons

become demagnetized such that the magnetic field can ultimately diffuse across the plasma and change topology. For the magnetic connectivity of electrons to change, it is required that $\mathbf{B} \times \left[\nabla \times (\mathbf{E} + \mathbf{v}_e \times \mathbf{B})\right] \neq 0$ (e.g., Hesse & Schindler, 1988; Vasyliunas, 1972). A necessary, but not sufficient, condition is thus that the electron flow must be nonideal, $\mathbf{E} + \mathbf{v}_e \times \mathbf{B} \neq 0$. Close to and inside the electron diffusion region, the electric field and sharply curved magnetic fields lead to complex electron trajectories (e.g., Bessho et al., 2014; Zenitani & Nagai, 2016). The detailed structure of electric and magnetic fields within an electron-scale current sheet have direct impact on the electron dynamics within the sheet. For example, in the presence of a guide magnetic field, the reconnection electric field has a component parallel to the magnetic field, and the outflow is focused to two opposing separatrices leading to an asymmetric flow pattern (e.g., Hesse et al., 2004; Pritchett & Coroniti, 2004; Wilder et al., 2017). At the same time, the electron dynamics provides feedback to the fields, which can lead to modification of the current sheet structure. One such modification is the bifurcation of the current sheet. Bifurcated current sheets are common in space, and while most observations report thicknesses comparable to ion length scales or larger (Asano et al., 2005; Gosling & Szabo, 2008; Hoshino et al., 1996; Retinò et al., 2007; Runov et al., 2003), some are comparable to electron scales (Burch & Phan, 2016; Wygant et al., 2005). In observations, the bifurcation is often attributed to the two slow shocks associated with a Petscheck-type reconnection exhaust (Gosling & Szabo, 2008; Hoshino et al., 1996).

In situ studies of electron dynamics within electron-scale current sheets in space have historically been challenging due to the severe constraint imposed by the temporal resolution of particle instruments. Many of these constraints have been lifted by the Magnetospheric Multiscale (MMS) mission (Burch et al., 2015), making the study of many aspects of electron-scale current sheets possible (Burch & Phan, 2016; Burch et al., 2016; Eriksson et al., 2016; Graham et al., 2017; Lavraud et al., 2016; Norgren et al., 2016). In this study, we report MMS observations of a bifurcated electron-scale current sheet with a finite guide field, embedded within a filamented dayside magnetopause current layer. We investigate the electron kinetic structure and magnetic connectivity, as well as signs of ongoing reconnection.

2. Observations

In this paper we use data from the MMS spacecraft, particle data from the Fast Plasma Investigation (FPI) (Pollock et al., 2016), magnetic field from the Fluxgate Magnetometer (Russell et al., 2014), and electric field from the Electric field Double Probe (Ergun et al., 2014; Lindqvist et al., 2014). All the times stated in the paper are in Coordinated Universal Time (UTC).

On 12 November 2015, MMS spent considerable time close to the subsolar point and made several crossings of the magnetopause. At the magnetopause crossings, the spacecraft observed mainly southward ion jets ($v_{i,z,\mathrm{GSE}} = -200$ to -400 km/s) as well as southward moving large-scale flux ropes, consistent with the existence of an X line located north of the spacecraft location. The last complete magnetopause crossing was associated with a wider and slower ion flow, $v_{i,z,\mathrm{GSE}} = -150$ km/s but had the largest current density. An overview of this last crossing is shown in Figure 1. At this time, MMS was located at [11.5, 2.8, −0.8] Earth radii in Geocentric Solar Ecliptic (GSE) coordinates and was in a tetrahedron formation with a separation of ~15 km. The average magnetic fields in the magnetosphere and magnetosheath were $\mathbf{B}_{\mathrm{MSP}} \approx [15, -5, 35]$ nT and $\mathbf{B}_{\mathrm{MSH}} \approx [0, 0, -20]$ nT (GSE; Figure 1a), respectively, corresponding to a magnetic shear angle of 150° across the magnetopause. The magnetosphere boundary is located at ~07:19:18 where the first spike in current density is observed (Figure 1b). The current density is calculated as $\mathbf{J} = n_e e(\mathbf{v}_\mathrm{i} - \mathbf{v}_\mathrm{e})$, where $\mathbf{v}_\mathrm{i}$ and $\mathbf{v}_\mathrm{e}$ are the ion and electron velocities, respectively, and n_e is the electron density, all calculated from the particle distributions sampled by FPI. To avoid errors associated with small differences between n_e and n_i, we use the electron density n_e for both the ion and electron contributions to the current. On the magnetospheric side of this boundary, the hot magnetospheric electrons can be seen at energies above 1,000 eV in the electron differential energy flux (DEF) spectrogram (Figure 1j). The spacecraft potential is marked with a black line, below which we observe photoelectrons originating from the spacecraft in the tenuous magnetospheric plasma environment. In the magnetosphere, there are also cold electrons and ions of magnetospheric origin (Figures 1i and 1j; e.g., Toledo-Redondo et al., 2016; Yau & André, 1997).

The magnetopause current layer, that is, the transition from the magnetosphere to the relatively unperturbed magnetosheath (roughly at around 07:19:38 where $\mathbf{B} \sim \mathbf{B}_{\mathrm{MSH}}$), is highly structured in the magnetic field (Figure 1a) with three additional regions of large current density $\mathbf{J}$ (Figure 1b). After the initial increase at about 07:19:16, the ion velocity remains relatively unperturbed throughout the boundary layer (Figure 1c).

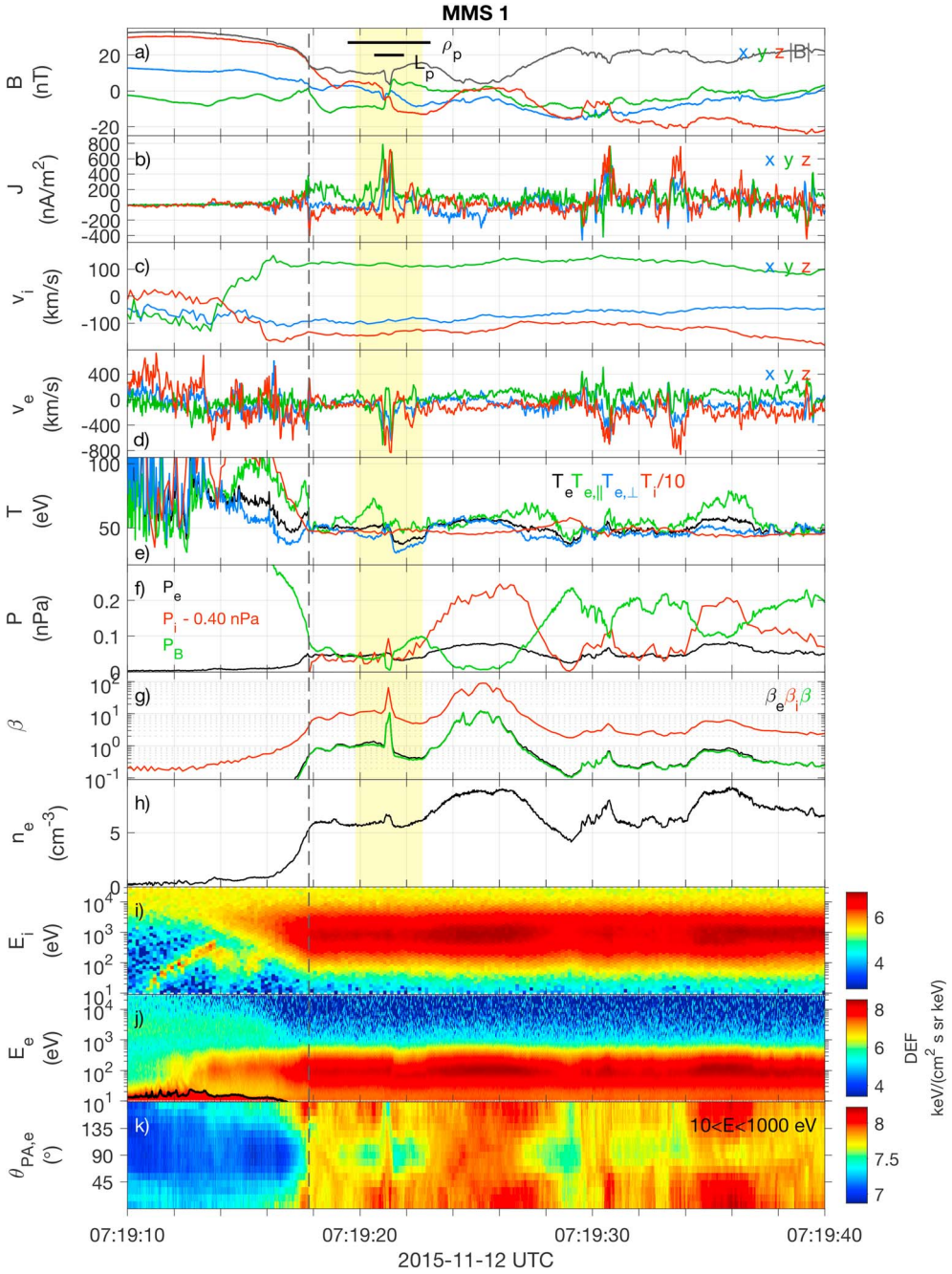

Figure 1. Overview of magnetopause crossing as seen by MMS1. All vectors are given in Geocentric Solar Ecliptic coordinates. The black-dashed line marks the magnetosphere boundary, and the yellow-shaded region marks the current sheet we study in detail. The proton gyroradius ρ_p = 250 km and proton inertial length L_p = 90 km are marked by black horizontal lines in panel a for reference. (a) Magnetic field. (b) Current density derived from ion and electron moments. (c) Ion velocity. (d) Electron velocity. (e) Total, parallel, and perpendicular electron temperatures and ion temperature divided by 10. (f) Electron and ion thermal pressures and magnetic field pressure. (g) Electron, ion, and total plasma beta. (h) Electron density. (i) Ion omnidirectional differential energy flux. (j) Electron omnidirectional differential energy flux. (k) Pitch-angle distribution of electron differential energy flux of energies between in the energy range 10 to 500 e 10 and 1,000 eV. MMS = Magnetospheric Multiscale; DEF = differential energy flux; UTC = Coordinated Universal Time.

The current filamentation is therefore due to the changes in electron velocity $\mathbf{v}_e$ (Figure 1d), as can be seen by comparing the structure of $\mathbf{v}_e$ to $\mathbf{J}$. The ion thermal pressure dominates both the electron thermal pressure ($T_i \approx 10T_e$; Figure 1e) and the magnetic field pressure (Figure 1f). While the total pressure remains constant when crossing the magnetospheric boundary (dashed line), it increases at around 07:19:22 (after yellow-shaded region). After this increase, the pressure remains constant throughout the rest of the crossing. The change in total pressure indicates that the magnetopause current layer could be influenced by some magnetosheath structure. The relatively large ion pressure is reflected in the plasma beta: $\beta_e \sim 0.1\beta_i \approx \beta \sim 1-10$, except for an interval of 4 s around 07:19:25 where $\beta_i \sim 10-100$. This means that, within the boundary layer, the available magnetic energy is small in comparison to the ion thermal energy but comparable or large in comparison to the electron thermal energy. We therefore expect the local energy conversion processes that transfer energy between the magnetic field and the plasma within the boundary layer, like magnetic reconnection, to have larger observable effect on the electrons. This is consistent with the lack of perturbation in the ion velocity.

Of the four current sheets, the second observed at about 07:19:21 (shaded yellow) has the largest magnetic shear $\Delta\theta_B \approx 120°$. In comparison, the first current sheet at the border of the magnetosphere has $\Delta\theta_B \approx 60°$, and the two last current sheets have $\Delta\theta_B \approx 30°$ and $\Delta\theta_B \approx 10°$. The second current sheet also has the largest magnetic curvature $\boldsymbol{\rho}_c = \left(\hat{b}\cdot\nabla\right)\hat{b}$ (shown in Figure 2h), where $\boldsymbol{\rho}_c$ is the curvature vector and $\hat{b} = \mathbf{B}/|\mathbf{B}|$ is the magnetic field unit vector. Large magnetic curvature indicates a nonplanar current sheet structure, where the field lines can connect the two sides of the current sheet. In such a current sheet, the magnetic tension can be released, as during magnetic reconnection (e.g., Biskamp, 2000, and references therein). The combination of relatively large magnetic shear, large magnetic field curvature, and large electron velocity indicates that this current might be the main location for the local release of magnetic field tension, the reconfiguring of the magnetic field, and the transfer of energy between the magnetic field and electrons in this boundary layer.

The pitch-angle distribution of electron DEF shows that throughout the boundary layer, the electron distribution is typically anisotropic (Figure 1k). Several regions with large transient temperature anisotropies $T_{e,\parallel} > T_{e,\perp}$ (Figure 1e) are present. One particular region is observed immediately after the second (largest shear) current sheet. Here the temperature anisotropy is due to a decrease of $T_{e,\perp}$ leading to a drop of T_e. In the center of this current sheet, $T_{e,\parallel} \approx T_{e,\perp}$ due to a local relative increase in $T_{e,\perp}$ associated with an enhancement of the electron DEF at perpendicular pitch angles (Figure 1k). Such an increase in $T_{e,\perp}$ and electron DEF around $\theta \sim 90°$ has been seen in both observations and simulations in the vicinity of the electron diffusion region of magnetic reconnection (Burch et al., 2016; Chen et al., 2016; Lavraud et al., 2016).

In the rest of this paper, we will investigate the second current sheet in more detail. We will investigate the electron dynamics within and in the vicinity of the current sheet and discuss whether or not magnetic reconnection is taking place. We will start in the next section by presenting the detailed observations of the current sheet.

3. Properties of the Largest Shear Current Sheet

In order to obtain a local coordinate system for the current sheet, we perform minimum variance analyses of the magnetic field and current density derived from the magnetic field for the time 07:19:20.116 to 07:19:22.136. All four spacecraft give similar results for the minimum variance analysis of the magnetic field, and we use the mean maximum variance direction for $\mathbf{L} = [0.14, -0.71, 0.69]$. The normal direction is $\mathbf{N} = \mathbf{L}\times\left(\mathbf{N}_J\times\mathbf{L}\right) = [0.81, -0.29, -0.47]$, where $\mathbf{N}_J = [0.84, -0.41, -0.36]$ is the minimum variance direction of the current computed using the curlometer method, and the third direction is $\mathbf{M} = \mathbf{L}\times\mathbf{N} = [-0.54, -0.62, -0.54]$. All coordinate vectors are given in GSE coordinates. In the remainder of the paper, unless otherwise stated, we will present all data in these LMN coordinates.

Figure 2 shows the spacecraft positions, magnetic fields, magnetic curvature, and current densities as observed by the four spacecraft. The magnetic fields are shown in Figures 2d–2g. The maximum variance component B_L reverses from $B_{in} \approx 9$ to -11 nT (Figure 2d). This field reversal is accompanied by a bipolar $B_M = \pm 5$ nT superposed on a guide field $B_G \approx 5$ nT $\approx 0.5B_{in}$ (Figures 2e-2f). At the center of the current sheet, a plateau is formed in both B_L and B_M. The magnetic field has a finite component in the normal direction $B_N \sim 1-2$ nT at the center of the current sheet (Figure 2g). This supports the notion that the two regions on opposite sides of the current sheet are magnetically connected. We note that B_N is small in comparison to B_L

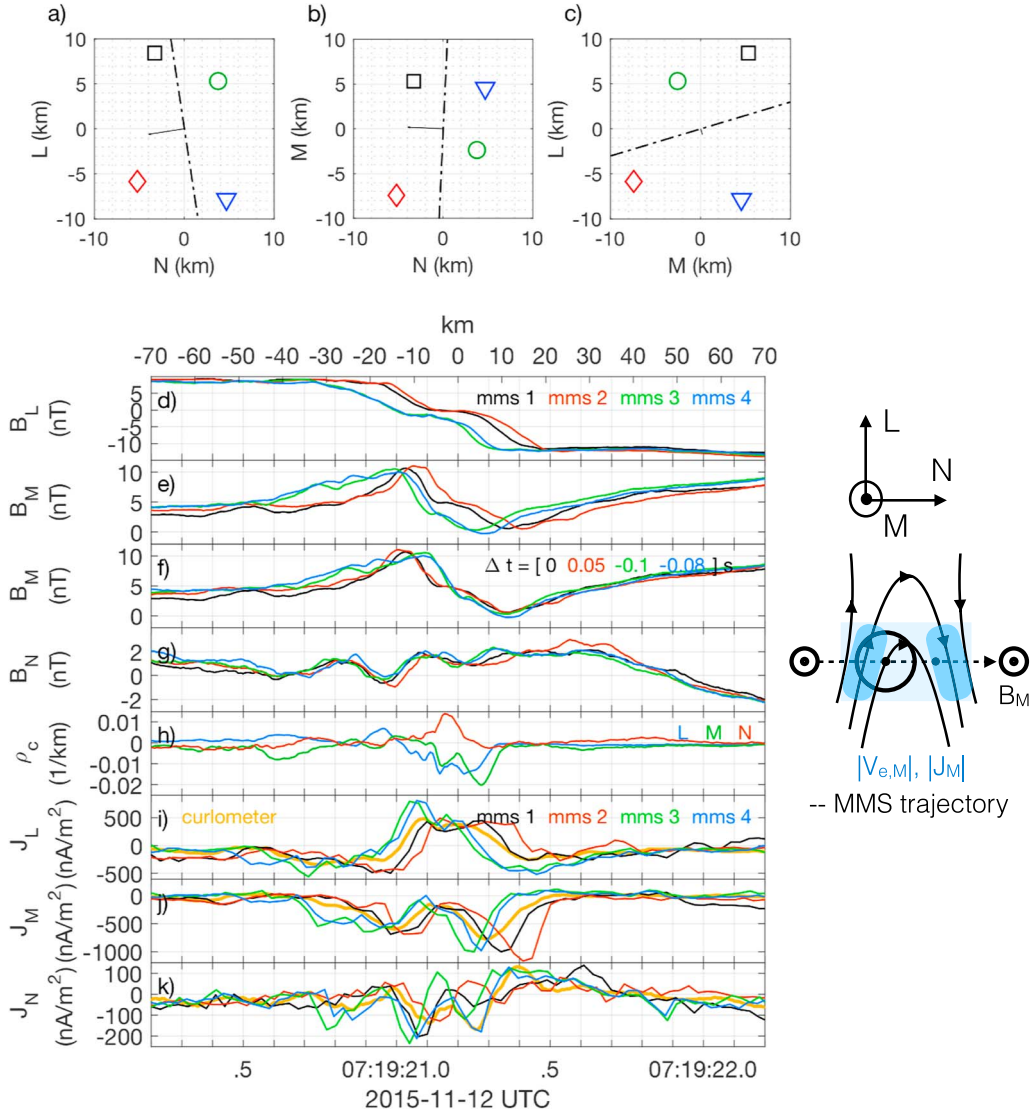

Figure 2. Structure of current sheet as seen by MMS1-4. (a)–(c) Spacecraft configuration. The dashed lines show the orientation and propagation direction of the boundary obtained from timing analysis. (d) B_L. (e) B_M. (f) B_M with shifted time lines corresponding to the velocity v_n of the current sheet. (g) B_N. (h) Magnetic curvature obtained from the four spacecraft. (i) J_L. (j) J_M. (k) J_N. The yellow line is the current derived from the magnetic field of the four spacecraft. (right) Sketch of in-plane (B_L and B_N, solid lines) and out-of-plane magnetic field (B_M, circles), current and electron flow bifurcation, and relative spacecraft trajectory. MMS = Magnetospheric Multiscale; UTC = Coordinated Universal Time.

and B_M, and the sign and amplitude of this component are therefore sensitive to small rotations of the coordinate system. However, a finite $B_N > 0$ is also consistent with the curvature of the magnetic field (Figure 2e) which starts by curving in toward the center of the current sheet and down in the direction of the electron flow (opposite to J_L in Figure 2i). Both $\rho_{c,L}$ and $\rho_{c,M}$ are larger on the right-hand side of the current sheet. However, while $\rho_{c,L}$ is only slightly asymmetric, the out-of-plane component of the magnetic field curvature $\rho_{c,M}$ is highly asymmetric. This is due to the combined effect of B_G and the bipolar part of B_M which adds up to 10 nT on the left side of the current sheet and cancel each other on the right side of the current sheet. The magnetic field unit vector $\hat{b}$ therefore turns from **M** in the center of the current sheet to **L** on the right-hand side over a distance of 10 km, resulting in large $\rho_{c,L}$ and $\rho_{c,M}$. The associated radius of curvature has a minimum value of $R_{c,\min} = 45$ km. However, since this quantity is derived from four spacecraft, it is possible that sharp turns in the magnetic field that occur on a scale smaller than the spacecraft separation are not properly captured.

We note that all four spacecraft observe similar fields but that they can be divided into two groups: MMS3-4 observes a slower decrease of B_L and a slightly larger J_L on the left side of the current sheet than MMS1-2.

To obtain an estimate of the length scale of the current sheet, we perform timing analysis of the observed fields. By assuming the current sheet is a planar 1-D structure and comparing the delay between the times the structure is observed by the different spacecraft, we can determine the velocity of the structure in its normal direction. By doing this for B_L, we obtain the average velocity $\mathbf{v}_n \approx 70 \times [-0.15, 0.04, -0.99]$ km/s (LMN), corresponding to a relative time delay $\Delta t_{\mathrm{MMS1\text{-}4}} = [0, 0.05, -0.10, -0.08]$ s for MMS1-4. The normal motion and alignment of the current sheet relative to the spacecraft are shown in Figures 2a–2c. Figure 2f shows B_M with the time lines shifted such that $t_{\mathrm{new}} = t - \Delta t$. We note that there is good correlation at the right side of the current sheet but a time delay of $\Delta T_{12-34} \sim 0.1$ s between MMS1-2 and MMS3-4 on the left side. This can be both due to temporal and transverse spatial variations.

The length scale calculated from $\boldsymbol{v}_n$ is shown on top of Figure 2d. The entire B_L reversal occurs over about 30 km, and the distance between the maximum and minimum values of B_M is ~20 km. As a reference to the scale of the current sheet, we have marked the ion inertial length $L_p = 90$ km and the ion gyroradius $\rho_p = 250$ km for protons in Figure 1a. The thickness of the current sheet is well below ion scales. Outside the current sheet, both the electron inertial length L_e and the electron gyroradius ρ_e are about 2 km. In the center of the current sheet, $L_e \sim 2$ km while $\rho_e \sim 7$ km. The thickness of the current sheet is thus on the same order as ρ_e but smaller than the minimal measured curvature radius $R_{c,\mathrm{min}}$.

Outside the current sheet, both electrons and ions move at the same velocity, frozen into the magnetic field, $\mathbf{E} + \mathbf{v}_{\mathrm{e,i}} \times \mathbf{B} = 0$. We therefore assume that the current sheet embedded in this flow move at the same velocity, $\mathbf{v}_{\mathrm{plasma}} \approx [-190, 50, -45]$ km/s (LMN), and we can estimate the relative transverse velocity to be $v_t = |\mathbf{v}_n - \mathbf{v}_{\mathrm{plasma},LM}| = 180$ km/s. The transverse distance covered during the time $T = 0.5$ s of the complete current sheet crossing is then $L_t = Tv_t \approx 90$ km. This is as also an estimate of the minimal transverse length of the current sheet.

Figures 2i–2k show the current densities, calculated from particle moments, as observed by the four spacecraft. The current density has a tripolar structure in the J_L component consistent with the Hall current system (Sonnerup, 1979). This current system is in turn consistent with the out-of-plane B_M, which we identify with the Hall magnetic field. The J_M component has a clearly bifurcated structure with a double peak associated with the plateau in B_L. We therefore conclude that the plateau in B_L is a spatial feature and not due to changes in the current sheet motion. The current density derived from the magnetic field is in good agreement with the average current density derived from the plasma moments of each spacecraft. The current component J_N in the direction normal to the current sheet shows some oscillations but is small relative to J_L and J_M as enforced from the choice of coordinate system.

Figures 3a–3d shows the magnetic field, electron velocity, and electric field as observed by MMS1 (MMS2 observes very similar fields). In the center of the current sheet, $v_{\mathrm{e},L} = -600$ km/s. The out-of-plane electron flow has two peaks $v_{\mathrm{e},M} \approx 700$ and 1,000 km/s, associated with the double peak in the current density, centered at the bipolar variations of B_M. By decomposing $\mathbf{v}_{\mathrm{e}}$ into perpendicular and parallel components, we can see how the flow is divided into comparably large $v_{\mathrm{e},\perp}$ and $v_{\mathrm{e},\parallel}$ (Figure 3c). The structure of the electron flow is bifurcated in both $v_{\mathrm{e},\parallel}$ and $v_{\mathrm{e},\perp}$, although their respective peaks are displaced with respect to each other. MMS3-4 only observes a distinct bifurcation in $v_{\mathrm{e},\perp}$, while $v_{\mathrm{e},\parallel}$ is wider and flatter with only a hint of bifurcation (shown for MMS 3 in Figure 5h). The perpendicular components of $\mathbf{v}_{\mathrm{e}}$ are divided between $v_{\mathrm{e},L}$ on the leftmost part and extending to the center of the current sheet and $v_{\mathrm{e},M}$ centered on the rightmost part of the current sheet.

To investigate if the electrons are frozen in to the plasma, we calculate the force terms in the electron momentum equation. The electron pressure divergence (Figure 3e) is calculated from the pressure tensor of the four spacecraft, and we compare its dominant normal component to the four spacecraft average of E_N and $(\mathbf{v}_{\mathrm{e}} \times \mathbf{B})_N$ in Figure 3f. We note that the double peak in $E_N + \left(\mathbf{v}_{\mathrm{e}} \times \mathbf{B}\right)_N$ at the right side of the current sheet is an artifact of the averaging because the scale size of the structure is comparable or smaller than the spacecraft separation (Figures 2a–2c). Figure 3g shows separately that $E_N + \left(\mathbf{v}_{\mathrm{e}} \times \mathbf{B}\right)_N \neq 0$ for all four spacecraft, with maximum values of about 5 mV/m, which is substantially larger than the maximum value in the averaged profile (in Figure 3f). Similarly, we expect the peak value of $\nabla \cdot \mathbf{P}_e/ne$ (in Figures 3e and 3f) to be underestimated. Within the errors of the measurements, $E_N + \left(\mathbf{v}_{\mathrm{e}} \times \mathbf{B}\right)_N + \left(\nabla \cdot \mathbf{P}_e/ne\right)_N = 0$. Considering the errors, the M and L components are insignificant. Neither can we identify any significant parallel component. Although the measurements clearly show that $\mathbf{E} + \mathbf{v}_{\mathrm{e}} \times \mathbf{B} \neq 0$, the calculations of $\nabla \times (\mathbf{E} + \mathbf{v}_{\mathrm{e}} \times \mathbf{B})$ and subsequently $\mathbf{B} \times \left[\nabla \times (\mathbf{E} + \mathbf{v}_{\mathrm{e}} \times \mathbf{B})\right]$ are very noisy throughout large parts of the boundary layer (not shown), and we do not

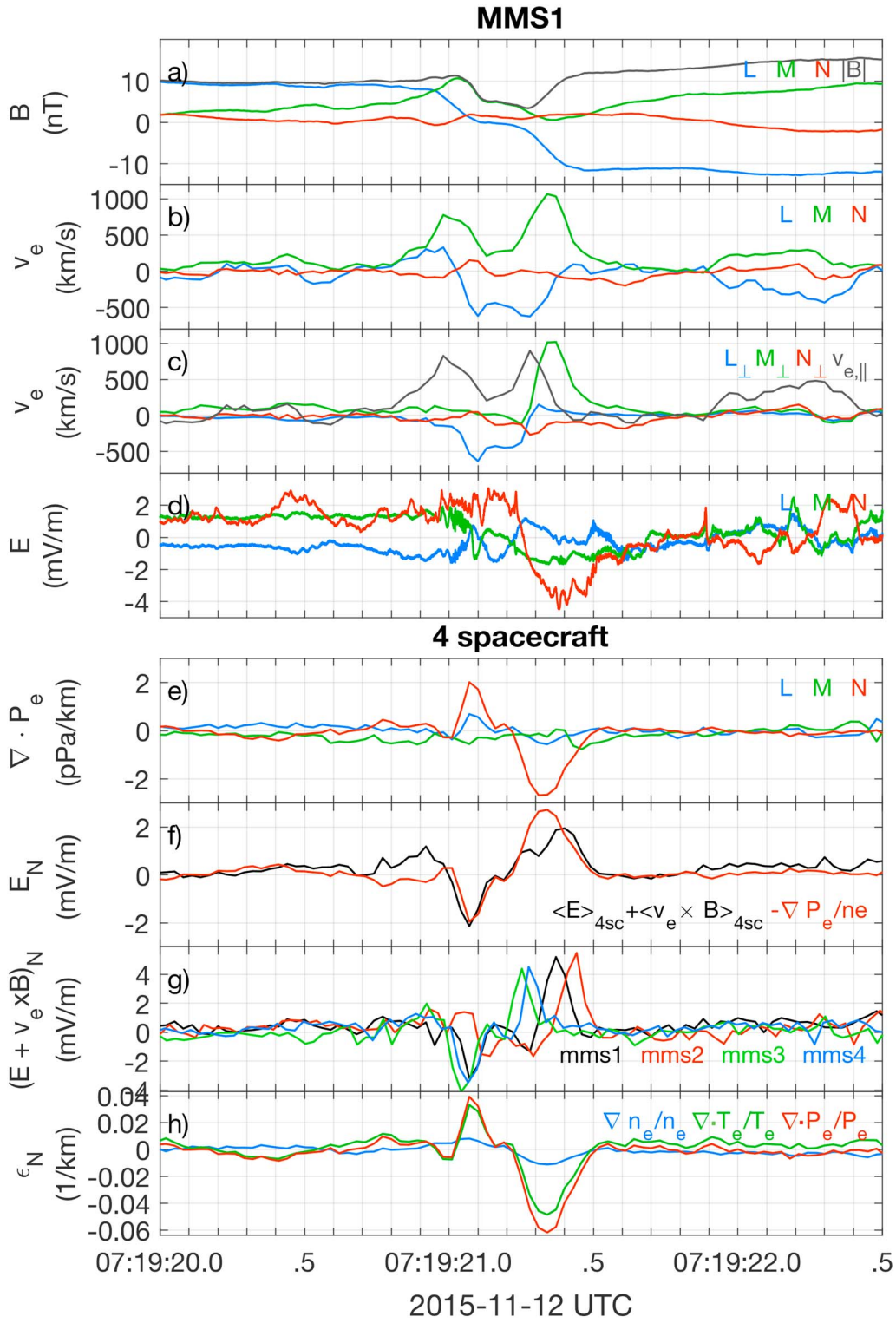

Figure 3. Structure of electron flow and forces at the current sheet as seen by MMS1 (a)–(d) and the four spacecraft (e)–(h). All vectors are in LMN coordinates. (a) Magnetic field. (b) Electron velocity. (c) Electron velocity decomposed into parallel and perpendicular components. (d) Electric field. (e) Electron pressure divergence. (f) Force terms in the electron momentum equation, $(\mathbf{E} + \mathbf{v}_e \times \mathbf{B})_N$ is approximately balanced by $(\nabla \cdot \mathbf{P}_e/ne)_N$. (g) Electric field in the electron frame $(\mathbf{E} + \mathbf{v}_e \times \mathbf{B})_N$ as seen by MMS1-4. (h) Inverse length scales of normal component of gradient of density ϵ_{n_e} and divergences of temperature ϵ_{T_e} and pressure ϵ_{P_e}. The temperature divergence contributes the largest part to the pressure divergence. MMS = Magnetospheric Multiscale; UTC = Coordinated Universal Time.

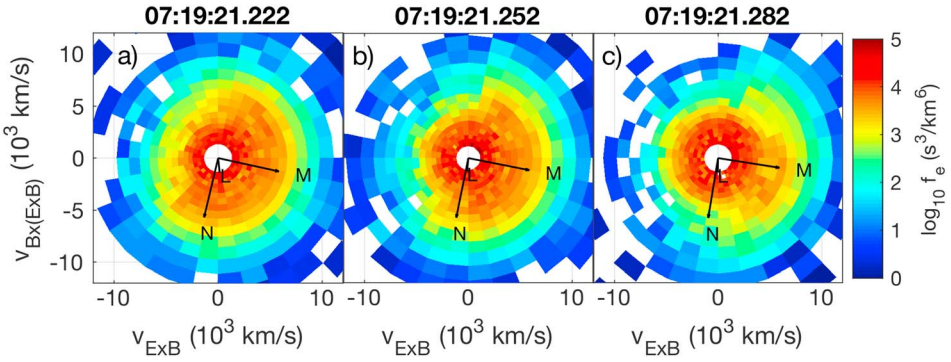

Figure 4. Evolution of phase space density of perpendicular electron distribution observed by MMS3 around the time of the largest amplitude $v_{e,M}$ on the right-hand side of the current sheet. The horizontal axis is the local $\mathbf{E}\times\mathbf{B}$ direction, while the vertical axis is the local $\mathbf{B}\times(\mathbf{E}\times\mathbf{B})$ direction. For reference, we have overplotted arrows marking the fixed LMN coordinate system. Further away from the center of the current sheet, the higher energy population (~5,000 km/s) covers a smaller azimuthal interval. This feature is consistent with the finite gyroradius effect observed both in simulations and observations of magnetic reconnection.

deem them reliable. We are also unable to calculate $\nabla\times(\nabla\cdot\mathbf{P}_e/ne)$ since $\nabla\cdot\mathbf{P}_e/ne$ is already a four-spacecraft quantity. Based on this analysis, we can therefore not determine if the motion of the electrons differ from the motion of the magnetic field (Vasyliunas, 1972).

Figure 3h shows the contributions to the pressure divergence $\epsilon_{P_e}=\epsilon_{T_e}+\epsilon_{n_e}$, where $\epsilon_{P_e}=3\nabla\cdot\mathbf{P}_e/\mathrm{trace}(\mathbf{P}_e)$, $\epsilon_{T_e}=3\nabla\cdot\mathbf{T}_e/\mathrm{trace}(\mathbf{T}_e)$, and $\epsilon_{n_e}=\nabla n_e/n_e$. The electron pressure divergence is mainly due to the electron temperature divergence and, to a smaller extent, the density gradient, indicating that heating may play a role in the current sheet. This large temperature divergence is associated with nongyrotropic electron distributions. Figure 4 shows three 2-D slices (with an angular opening of ±15°) of the electron distributions in the plane perpendicular to the magnetic field observed by MMS3 at the time of largest amplitudes $v_{e,\perp,M}$ at the right-hand side of the current sheet (see Figure 5h). The planes are defined by the vectors $\mathbf{E}\times\mathbf{B}$ and $\mathbf{B}\times(\mathbf{E}\times\mathbf{B})$, with $\mathbf{B}$ directed out of the plane. The fixed LMN coordinate system is overplotted for reference. All three distributions show nongyrotropic features at higher energies (~5,000 km/s). The azimuthal coverage of these populations becomes progressively smaller the further away from the current sheet center we move. This behavior is consistent with the finite gyroradius effects reported both in observations and simulations of magnetic reconnection (Burch et al., 2016; Hesse et al., 2014; Norgren et al., 2016). Recently, Rager et al. (2018) demonstrated that the electron crescent distributions observed by MMS can be considered as manifestations of the electron diamagnetic drift. Although the nongyrotropic electron distributions in this current sheet do not form distinct crescents, the underlying physics is same. Similar, but less distinct, nongyrotropic features are also observed on the left-hand side of the current sheet. MMS4 observes similar distributions as MMS3. MMS1 and MMS2 observe similar distributions as MMS3 and MMS4 on the right side of the current sheet, while the distributions on the left side of the current sheet observed by MMS1 and MMS2 only show vague nongyrotropic features.

From the analysis in the two previous paragraphs, we were only able to get an idea of the nature of the perpendicular electron flow. We did not address the origin of the warmer perpendicular population constituting the nongyrotropic features nor could we investigate the parallel electron flow in any detail. In order to examine the electron dynamics in more detail and search for signs of ongoing magnetic reconnection, we will therefore perform test particle simulations and compare the results with observations in the following sections.

Before we continue with more detailed analyses and discussions of the current sheet properties, we make a comment on the electric field (Figure 3d). None of the electric field components had large amplitudes. In fact, their amplitudes are close to the errors (~2 mV/m) of the electric field instrument at these low frequencies. However, the electric field component E_N normal to the current sheet could be associated with other independent measurements, namely, the other force terms in the electron momentum equation, $\left(\mathbf{v}_e\times\mathbf{B}\right)_N$ and $\left(\nabla\cdot\mathbf{P}_e/ne\right)_N$. We therefore deem E_N reliable. The other components of the electric field, E_M and E_L, have amplitudes comparable or even smaller than E_N. And unlike what we could do for E_N, we could not relate them to their respective components in the electron momentum equation. This is also true for an eventual parallel electric field component $E_{||}$. Therefore, in section 4.3, we will take a different approach to examine the possible presence of an out-of-plane electric field E_M.

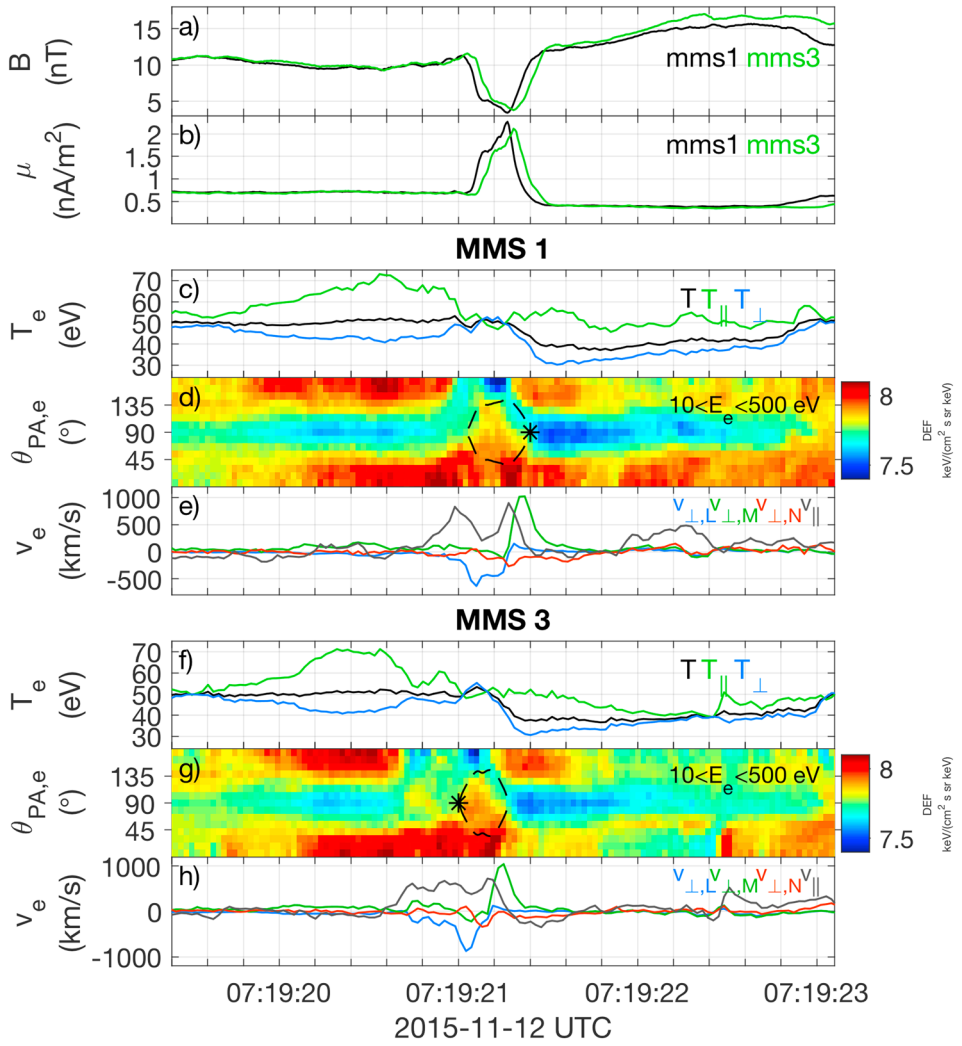

Figure 5. (a) Magnetic field amplitude. (b) Magnetic moment based on perpendicular thermal velocity of electrons. (c) and (f) Electron temperature. (d) and (g) Pitch-angle distribution of electron differential energy flux in the energy range 10 to 500 eV. The dashed lines mark the expected variation in pitch angle for adiabatic electrons θ_m, see equation (1). (e) and (h) Electron velocity decomposed into parallel and perpendicular components. MMS = Magnetospheric Multiscale; UTC = Coordinated Universal Time.

In summary, we observe an electron-scale current sheet embedded within a filamented magnetopause current layer of several ion-scale thickness. The electron-scale current sheet has a guide magnetic field $B_G = 0.5B_{in}$, bifurcated structure, and comparably large parallel and perpendicular currents carried primarily by electrons. The perpendicular electron flow is balanced approximately equally by the electric field and electron pressure divergence.

4. Discussion

We have presented observations of a bifurcated current sheet with thickness comparable to electrons scales, with both parallel and perpendicular electron flows and currents. In this section we will further discuss and investigate the electron dynamics in the vicinity and within the current sheet, and how they manifest in the data. We will also discuss what signatures can be interpreted as signs of magnetic reconnection.

Since the current sheet was not located directly at the magnetopause but was embedded into the magnetopause boundary layer, plasma beta in the immediate vicinity of the current sheet was relatively large, $\beta_i \approx 5-15$, while $\beta_e \approx 0.5-1.5$. Therefore, if magnetic reconnection is indeed ongoing in the current sheet, we expected it to have larger observable effects on the electrons, which is consistent with the lack of perturbation

in the ion velocity in the vicinity of the current sheet. However, it is also possible that the observations were made close to the EDR and that the ion jet was not fully formed (Wilder et al., 2017) or that the neighboring magnetic and plasma topology prevented the formation of a large-scale ion jet (Phan et al., 2018). In this event, since we do observe a weak ion jet on a larger scale, it is possible that the current sheet is embedded in a larger-scale ion exhaust, similar to the simulations by Daughton et al. (2011).

The electron flow in the outflow direction peaked at $v_{e,L} = -600$ and $-1,000$ km/s for MMS1-2 and MMS3-4, respectively. The expected magnetic reconnection electron outlow speed close to the electron diffusion is expected to scale with the electron Alfvén speed $v_{A,e} = B/\sqrt{\mu_0 n m_e}$, where B and n are taken in the electron inflow region (Shay et al., 2001). Shay et al. (2001) gives $v_{out} \sim v_{A,e} L_e/l$, where l is the half thickness of the current sheet and $L_e = c/\omega_{pe}$ is the electron interial length inside the current sheet. In the vicinity of the current sheet, $v_{A,e}$ varies between ~4,000 km/s on the left side and ~5,000–6,000 km/s on the right side of the current sheet, $l = 16$ km and $L_e \approx 2$ km both inside and outside the current sheet. As a result $v_{out} \approx$ 500–750 km/s, which is consistent with the observed values. Assuming a dimensionless reconnection rate of $R = v_{in}/v_{out} = 0.1$, the inflow speed should be $v_{in} \approx 50$–75 km/s. Due to the relatively low expected value of v_{in} in conjunction with the errors associated with both the particle instrument and the chosen coordinate system of the current sheet, v_{in} cannot be reliably determined from measurements.

The reconnection electric field associated with the estimated inflow speed is $E_r \sim v_{in} B_{in} \sim 0.5$ mV/m, where $v_{in} = 50$ km/s is taken from the last paragraph and $B_{in} \approx 10$ nT is the amplitude of the magnetic field adjacent to the current sheet. The existence of such a small amplitude, low frequency, electric field is not possible to infer from the electric field measurements due to instrument uncertainties. However, if such an electric field is indeed present inside and/or in the vicinity of the current sheet, there might be observable signatures in the electron data. To investigate this, we will first investigate the adiabatic behavior of electrons. Thereafter, we will consider the nonadiabatic effects due to magnetic curvature and electric fields on the electron trajectories.

4.1. Electron Dynamics: Adiabatic Electron Motion

We start by investigating the behavior of electrons in the regions outside the current sheet. In these regions, the magnetic field amplitude B changes slowly (Figure 5a), and the magnetic moment based on $T_{e,\perp}$: $\mu_{T_e} = k_B T_{e,\perp}/B$ is constant on the left and right side of the current sheet (Figure 5b). This indicates that the electrons behave adiabatically here. Since μ_{T_e} is constant, the change in B is accompanied by a change in $T_{e,\perp}$ (Figures 5c and 5f), as the electrons are focused along the weakening magnetic field. At the same time, in the adiabatic regions, $\mathbf{E} + \mathbf{v}_e \times \mathbf{B} = 0$ (Figure 3g), and therefore, the motion of the electrons is tied to the motion of the magnetic field lines.

The gradient in B, and subsequent change in $T_{e,\perp}$, is most prominent on the right-hand side of the current sheet. Here $T_{e,\perp}$ changes monotonically from 40 eV at the outer edge of the adiabatic region to 30 eV at the inner edge. This continuous change indicates that electrons tied to adjacent magnetic field lines (or flux tubes) are from a common source region and have undergone similar processes but are in different stages of progression, either temporally, spatially, or a combination thereof. Since the behavior of the majority of electrons in this region outside the center of the current sheet is adiabatic, the process related to the trend observed in $T_{e,\perp}$ is in principle reversible. However, if the electrons drift with the magnetic field inward toward the current sheet edge, and there become scattered in the curved magnetic field, the process is more likely to be irreversible. If this is the case, the signatures of the adiabatic region are consistent with the inflow region of magnetic reconnection. We will examine the behavior of the electrons at the edge of the current sheet in section 4.2.

In the center of the current sheet, the magnetic moment is not constant, and we investigate to what extent the electrons bounce adiabatically in the magnetic field minimum. For adiabatic motion in a magnetic minimum, the variation of the pitch-angle distribution can be described by the angle

$$\theta_m = \sin^{-1}\left(\sqrt{\frac{B}{B_{ref}}}\sin\theta_{ref}\right). \quad (1)$$

This predicted pitch-angle variation θ_m for the inner part of the current sheet is plotted as dashed lines in Figures 5d (MMS1) and 5g (MMS3). The star (∗) marks the time where $B_{ref} = 14$ nT and $\theta_{ref} = 90°$ are taken. The broadening of the observed electron pitch-angle distribution is only roughly traced by the value predicted by equation (1), regardless of energy range (not shown). In fact, the entire population is shifted toward

$\theta = 0°$. This behavior is different from the observations by Lavraud et al. (2016), where the electron population bouncing in the magnetic field minimum was symmetric about $\theta = 90°$. The partial fit to θ_m indicates two things. First, some, but not all, of the electrons behave adiabatically in the inner region, bouncing in the magnetic field minimum. Second, the electron population is not only affected by the magnetic field but probably also by some electric field. In the next section we will investigate the electron dynamics that are not related to adiabatic motion. This includes the transition between the outer regions and the center of the current sheet in section 4.2 and the effects of an out-of-plane electric field in section 4.3.

4.2. Electron Dynamics: Curved Magnetic Field

As deduced from timing analysis, the current sheet thickness was on the order of the local thermal electron gyroradius, which varied between 2 and 7 km between the edge and the center of the current sheet. It is thus likely that the electrons can cross a large part of the current sheet during one f_{ce}^{-1} and meanwhile experience large changes in the magnetic field. On the other hand, the minimal magnetic curvature radius was $R_{c,\min} = 45$ km, which indicates that the electron trajectories should be nonchaotic (Buechner & Zelenyi, 1989). However, since the magnetic curvature is derived from four spacecraft, it is possible that it does not properly capture the sharpest magnetic field curvatures that occur on scales below the spacecraft separation. Therefore, to examine the dynamics of the electrons in the curved magnetic field, we perform test particle integrations in a 1-D magnetic field model based on the observed data: $\mathbf{B}(N)$. By using a model magnetic field that only varies in the normal direction N, we have assumed that the current sheet is translationally invariant along M and L. The model is based on two Harris current sheets that, in order to create the bifurcated structure, are displaced with respect to each other in the normal direction. The out-of-plane magnetic field is constructed by a constant guide field and two Gaussians to represent the Hall field, also displaced with respect to each other to create the bifurcation, while the normal magnetic field is kept constant:

$$B_L^{\mathrm{mod}} = B_0 + B_{0,1}\tanh\left(\frac{N-N_1}{a_1}\right) + B_{0,2}\tanh\left(\frac{N-N_2}{a_2}\right), \tag{2}$$

$$B_M^{\mathrm{mod}} = B_G + B_{H,1}\exp\left(-\frac{(N-N_3)^2}{a_3^2}\right) + B_{H,2}\exp\left(-\frac{(N-N_4)^2}{a_4^2}\right), \tag{3}$$

$$B_N^{\mathrm{mod}} = B_n, \tag{4}$$

where $B_0 = -1.5$ nT, $B_{0,1} = -4.5$ nT, $B_{0,2} = -5.5$ nT, $B_G = 5$ nT, $B_{H,1} = 5.5$ nT, $B_{H,2} = -4.5$ nT, $B_n = 1.5$ nT, $N_1 = N_3 = -11$ km, $N_2 = 11$ km, $N_4 = 14$ km, $a_1 = a_2 = a_3 = 5$ km, and $a_4 = 8$ km. These values are chosen to provide a good fit to the magnetic field observed by MMS1. Figure 6a shows the comparison between the model magnetic field (dashed lines) and the observed magnetic field (solid lines). Since the current sheet is bifurcated, we define the half width l as half the displacement of the two Harris current sheets we used to construct B_L^{mod} plus their average individual half width: that is, $l = (N_2 - N_1 + a_1 + a_2)/2 = 16$ km. For these parameters, we can calculate the curvature parameter as defined by Zenitani et al. (2017; we have rewritten their equation 2 explicitly in terms of the different components of B^{mod}): $\kappa_{\mathrm{tot}} = \frac{|B_n|}{|B_{0,1}+B_{0,2}|}\left(\frac{l}{\rho_0}\right)^{1/2}\left(1+\left|\frac{B_G}{B_n}\right|^2\right)^{3/4} = [1.2, 1.0, 0.8]$, where $\rho_0 = [2.1, 3.4, 4.8]$ km is the gyroradius about the reference magnetic field $B_{0,1} + B_{0,2}$ for an electron with energy [40, 100, 200] eV, respectively. Since $\kappa_{\mathrm{tot}} \sim 1$ for all of these energies, we expect electrons belonging to a large energy range to have chaotic trajectories. For now, we start by solely investigating the effect of the magnetic field on the particles, and we keep the electric field in the model, $\mathbf{E}^{\mathrm{mod}} = 0$. We start by showing the behavior of four example electrons and thereafter go on to include a larger number to generalize the results. We shall see that the magnetic field structure leads to different behavior of electrons entering from opposite sides of the current sheet.

Figures 6h–6j show the trajectories of four electrons; two originating from the left (blue and green) and two originating from the right (red and black) of the current sheet. For reference, two magnetic field lines based on the model are shown in yellow. The pitch angle of the electrons throughout their trajectories are overlaid on the pitch-angle spectrogram of the observed phase space density (PSD) in Figure 6d. Figure 6c shows the same spectrogram without the overlaid electron pitch angles. The initial pitch angles are close to field aligned, and the energies are $E = 40$ eV (thermal) and $E = 170$ eV. While the trajectories of the electrons entering from the same side but with different energies are similar, the trajectories of the electrons entering from opposite sides are disparate. This is a direct consequence of the curvature of the magnetic field. The amplitude of the

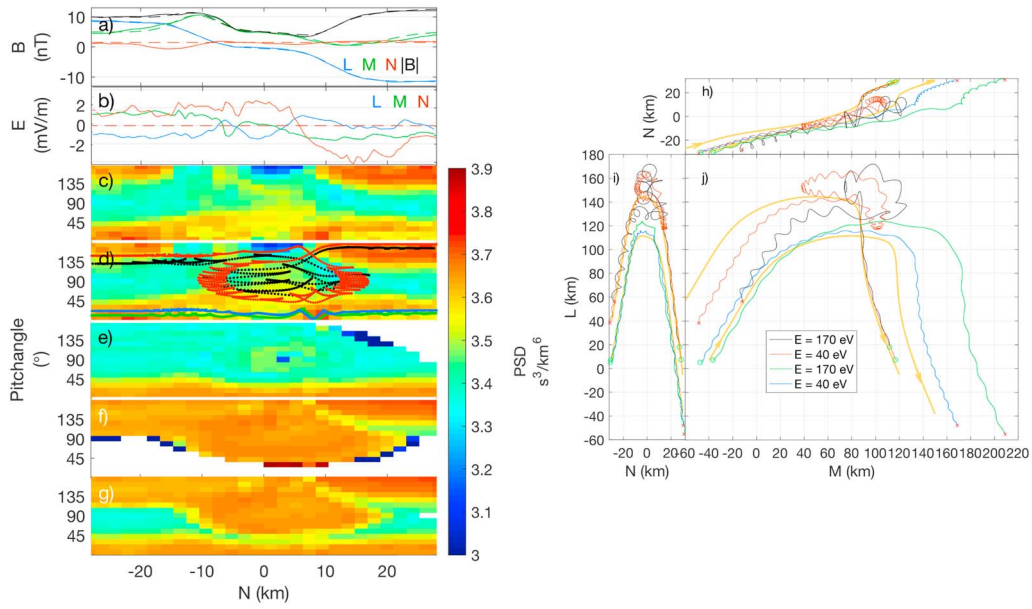

Figure 6. Test particle integration with $\mathbf{E}^{\mathrm{mod}} = 0$. (a) Observed (solid) and model (dashed) magnetic field. (b) Observed (solid) and model (dashed) electric field. (c) Observed pitch-angle spectrogram of electron PSD. (d) Same as (c) but with overlaid pitch angle and normal position of the four test particles shown in (h)–(j). (e) Electron test particles originating from the left. (f) Electron test particles originating from the right. (g) All test electrons originating from both left and right. (h–j) Example electron trajectories, two originating from left and two from the right. The green circle (red cross) marks the starting (stopping) locations. Magnetic field lines based on the model is shown in yellow. The magnetic field curvature is larger at $N > 0$. Therefore, electrons entering the current sheet from this side are scattered to perpendicular pitch angles on their inbound leg and form the perpendicular population observed in the center of the current sheet. Electrons entering from $N < 0$ are scattered on their outbound leg and can therefore remain relatively field aligned during the crossing. PSD = phase space density.

guide magnetic field ($B_G \approx 5$ nT) is similar to the Hall magnetic field ($B_H \approx \pm 5$) such that the out-of-plane magnetic field B_M adds up to 10 nT on the left side of the current sheet and vanishes on the right side of the current sheet. This results in a kink in the magnetic field on the right side, with the associated magnetic curvature being greater. The electrons that enter from the side of least curvature (left side) manage to follow the magnetic field on their inbound trajectory because their gyroradius is smaller than the curvature radius. At the center of the current sheet, their motion is still orderly and trace the magnetic field with little change in pitch angle, $\theta \sim 0°$. As they reach the side of the largest curvature (right side), they are deflected in the curved magnetic field and temporarily reach slightly more perpendicular pitch angles ($\theta \sim 40°$; see Figures 6h and 6i at $N = 10$ km and $L = 110$ km) before they are ejected from the current sheet along the magnetic field. The electrons originating from the side of the largest curvature (right-hand side) are deflected to perpendicular pitch angles ($60° \lesssim \theta \lesssim 140°$) in the largely curved magnetic field on the inbound leg of their trajectory. Therefore, they enter the center of the current sheet at large pitch angles and are reflected back and forth before they exit the current sheet along the magnetic field on the left side.

We have extended this analysis by tracing a total of $N_e = 2 \times N_\theta \times N_\phi \times N_E = 18,432$ electrons in the model magnetic field, half of which are entering from the left and half from the right. The electrons cover $N_\theta = 12$ pitch angles in the range $\theta = [0°, 90°]$ (left) and $[90°, 180°]$ (right), $N_\phi = 24$ azimuthal angles (angles perpendicular to **B**), and $N_E = 32$ energy levels in the range $E = [14, 670]$ eV. We let each electron represent an ensemble of electrons with similar **v** at the beginning of the trajectory. For each electron and its corresponding trajectory, we assume $df/dt = 0$ and assign the phase space density as measured by FPI at the starting location for the closest corresponding velocity. The results are shown as PSD in Figures 6e–6f, for the energy range [30, 300] eV. This energy range is smaller than the range of initial energies to account for the change of energy related to the interaction of the electrons with $\mathbf{E}^{\mathrm{mod}} \neq 0$ as we will study later. We apply this limited energy range for $\mathbf{E}^{\mathrm{mod}} = 0$ to make the comparison more straightforward.

Figure 6e shows the mapping of the electrons entering from the left. At the edge of the current sheet where the magnetic field has a local maximum ($N = -10$ km), the electrons go to slightly larger pitch angles. In

the center of the current sheet, they are focused along the weakening magnetic field. At the right side of the current sheet, most of the electrons are ejected, while a few are reflected and exit at the side from which they came.

Figure 6f shows the mapping of electrons originating from the right. As the electrons approach the current sheet edge, they are focused along the magnetic field. At the current sheet edge ($N = 10$ km), they are deflected from $\theta \sim 0°$ to $\theta \sim 90°$ in the highly curved magnetic field. Inside the current sheet, the electrons bounce in the magnetic field minima before they exit on the left-hand side, less focused along the magnetic field as opposed to when they entered. The initial deflection from $\theta \sim 0°$ to $\theta \sim 90°$ is quantitatively consistent with the observations (Figure 6c), and we therefore conclude that the electrons entering from the side of the largest curvature constitute the major part of the perpendicular electron population present at the center of the current sheet. The PSD of the test particles in the center of the current sheet is approximately symmetrical around $\theta \sim 90°$. This is not consistent with the observations that has a depletion of PSD (and DEF) at $\theta = 180°$ in the center of the current sheet. This depletion also extends to the left-hand side of the current sheet as is seen most prominently in the DEF for MMS3 in Figure 5g. We therefore conclude that the behavior in the center of the current sheet and exit of electrons on the left side of the current sheet is not accurately modeled. We will investigate the cause of this below, including the effect of the electric field. Figure 6g shows the combined test particle PSD of electrons entering from both left and right. We note that the two populations remain relatively well separated.

4.3. Electron Dynamics: Finite Electric Field E_M

The observed signature of the electron distribution that could not be explained by the magnetic field alone was the asymmetry in PSD (and DEF) between $\theta = 0°$ and $\theta = 180°$ in the center and slightly to the left edge of the current sheet. As the electron population was shifted toward $\theta = 0°$ in the center of the current sheet, we would expect an electric field at the center of the current sheet to be directed antiparallel to the magnetic field, that is, along $\sim -\boldsymbol{M}$. That is, since the electrons entering from the right side of the current sheet travel antiparallel to **B**, they would experience a decelerating force due to this electric field. We note that the direction of $E_M < 0$ is consistent with the expected direction of the reconnection electric field in this topology. In the remainder of this section, we will therefore investigate more quantitatively what effect an electric field $E_M < 0$ would have on the electrons. To simplify the following modeling, we have chosen a simple 1-D electric field model in which $E_L^{\mathrm{mod}} = E_N^{\mathrm{mod}} = 0$, and E_M^{mod} tends to zero outside the current sheet. We motivate the relevance of this simplified model in the following way: In the reconnection picture, outside the diffusion regions, the electric field is perpendicular to **B** and associated with the convection of plasma in toward the diffusion regions (e.g., Hesse et al., 2004). Inside the diffusion regions where the particles become demagnetized, the electric field-particle interaction becomes more complicated and can result in finite acceleration and energy conversion between the magnetic fields and particles. By applying this simplified model, we thus neglect the motional electric field associated with convection in the inflow regions but retain the diffusive electric field associated with the change of magnetic topology and connectivity of particles.

The out-of-plane electric field is given by

$$E_M^{\mathrm{mod}} = E_m \exp\left(-\frac{(N - N_5)^2}{a_5^2}\right), \tag{5}$$

where $N_5 = 5$ km, $a_5 = 12$ km, and $E_m = -1$ mV/m (Figure 7b), comparable to the expected reconnection electric field. We have chosen to center the electric field slightly to the right of the current sheet center since the perpendicular population as mapped in the previous section was also centered slightly to the right of the center. However, we note that $N_5 = 0$ gives qualitatively similar results (not shown). The trajectories of the same four electrons as for the case of no electric field (Figure 6) are shown in the same format in Figures 7h–7j. We can see that the electric field confines the red and black electrons to the right side of the center of the current sheet. They are initially decelerated and then reflected back toward the right, where the red one exits and the black one mirrors and repeats the procedure before it exits at the same side it entered from. Both particles exit the current sheet further downstream ($-\boldsymbol{L}$) and further out along $\boldsymbol{M}$ from where they entered. This general direction of motion is consistent with the observed electron velocities (e.g., Figure 3b). The green and blue electrons entering from the left are instead accelerated as they cross the current sheet and exit on the right.

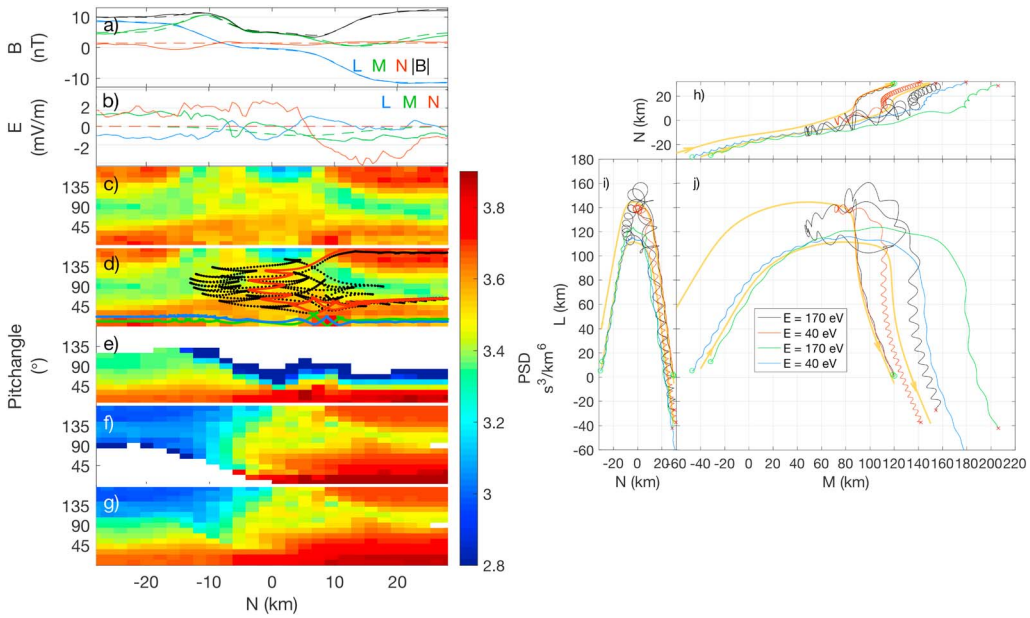

Figure 7. Test particle integration with $\mathbf{E}^{\mathrm{mod}} \neq 0$. (a) Observed (solid) and model (dashed) magnetic field. (b) Observed (solid) and model (dashed) electric field. (c) Pitch-angle spectrogram of electron PSD. (d) Same as (c) but with overlaid pitch angle and normal position of the four test particles shown in (h)–(j). (e) Electron test particles originating from the left. (f) Electrons test particles originating from the right. (g) All test electrons originating from both left and right. (h–j) Example electron trajectories, two originating from left and two from the right. The green circle (red cross) marks the starting (stopping) locations. Magnetic field lines based on the model is shown in yellow. The electric field $E_M < 0$ prevents electrons entering from $N > 0$ to exit on the opposite side. Electrons entering from $N < 0$ are instead accelerated during the crossing. PSD = phase space density.

For this case with $E_M^{\mathrm{mod}} \neq 0$, we use the same method to map the electron PSD as for the case with $E_M^{\mathrm{mod}} = 0$. Electrons entering from the left are accelerated by E_M^{mod} at the center of the current sheet and exit on the right side (Figure 7e). At around $N = 4-5$ km, the electrons are temporarily deflected to slightly larger pitch angles as they encounter the largely curved magnetic field and are thereafter ejected. This effect was not apparent in the mapped PSD for $\mathbf{E}^{\mathrm{mod}} = 0$ (Figure 6e), probably because the electrons were not accelerated prior to the deflection. In Figure 7f, we can see that most electrons coming from the right remain in the center of the current sheet before they are reflected back out the way they came. This reflection due to the electric field results in a distinct depletion of both PSD and DEF (not shown) around $\theta = 180°$ in the center and on the left edge of the current sheet (Figures 7f and 7g). In the observations, this depletion is seen by all spacecraft to different extents. The most distinct depletions are seen by MMS3-4, as can be seen in the DEF for MMS3 in Figure 5g.

Figure 7g shows the mapping for all the electrons. Based on the similarities seen between the mapped and the observed data, we draw the conclusion that the depletion of PSD at the left side of the current sheet can be explained by an out-of-plane electric field E_M. That is, the electron mapping suggests there is a small $E_{\parallel}$, consistent with the reconnection electric field (e.g., Pritchett & Coroniti, 2004), present in the observed current sheet. As a result of this electric field, there is an excess of electrons moving parallel to **B** on the left side of the current sheet, explaining the parallel electron flow there. The parallel electron flow on the right side of the current sheet can be explained by the acceleration of the electrons as they pass the central current sheet. This parallel electron flow pattern is consistent with the electron flow in numerical simulations of guide field reconnection (e.g., Pritchett & Coroniti, 2004). We thus propose that these signatures in the electron data are manifestations of ongoing reconnection. And we identify E_M with the reconnection electric field.

The comparison between the observed and mapped PSD, however, is understandably not perfect. The large difference between the observed and modeled data is the number of electrons exiting on the right side of the current sheet. We believe this to be a shortcoming of the 1-D model, that is, that the actual current sheet is not entirely invariant in *L*. Since we employ a 1-D model, the only direction in which the electrons can enter and exit the current sheet is the normal direction *N*. As the particles entering from the right are not exiting on the left side due to E_M, they have to exit on the right. This would lead to an accumulation of PSD and DEF

on the right side, which we do not observe in the data (Figure 7c). This suggests that in the actual current sheet, electrons are convected away in the outflow along $-\boldsymbol{L}$ or $\boldsymbol{M}$ (assuming the current sheet is finite in the out-of-plane direction), in the directions of $\mathbf{v}_e$ (see, e.g., Figure 3b). That is, the current sheet could be a channel that removes electrons from the two outer regions, consistent with the magnetic reconnection picture. If this is the case, it indicates the inflow regions extend over the entire adiabatic regions, since the shift in pitch angle was continuous.

Another difference between the observed and mapped PSD is the repopulation of electrons at $\theta \sim 180°$ at $N \approx -15$ km. This repopulation is likely due to electrons bouncing parallel to the magnetic field in the inflow region (Egedal et al., 2009) and is not well described by the simple model we apply.

4.4. Current Bifurcation

In this study, we have shown that the detailed structure of electric and magnetic fields within an electron-scale current sheet have direct impact on the electron kinetics within the sheet. At the same time, such electron kinetics provides self-consistent feedback to the fields, which can lead to modification of the current sheet structure. From the observations, we could see that the bifurcation observed by MMS1-2 was due to currents carried by both $\mathbf{v}_{e,\perp}$ and $\mathbf{v}_{e,\parallel}$. For MMS3-4, the bifurcation was mainly due to $\mathbf{v}_{e,\perp}$. The perpendicular flows were supported by a combination of E_N and $\left(\nabla \cdot \mathbf{P}_e\right)_N$ on either side of the current sheet. Since both E_N and $\left(\nabla \cdot \mathbf{P}_e\right)_N$ vanish at the center of the current sheet, this leads to a bifurcated electron flow and current density. This is similar to the recent observation by Wang et al. (2018), although in that event the bifurcation was less distinct and only due to E_N. Since finite E_N can readily form in nonreconnecting current sheets, the perpendicular bifurcation of this particular current sheet could be explained by the quasi-steady compression as hypothethized by Schindler and Hesse (2008). In their study, the bifurcation could form without the need of a finite B_N or magnetic reconnection. On the other hand, the description of perpendicular flow is also consistent with the simulation of reconnection onset by Liu et al. (2014). There the bifurcated current was carried by nongyrotropic components of the electron population. The nongyrotropic electrons were attributed to the finite gyroradius excursions of the heated electrons from the center of the current sheet.

The bifurcation due to parallel electron flows, as inferred from the particle tracing in section 4.3, could be attributed to the presence of an electric field with dominant parallel component in the center of the current sheet. The electric field provided a potential ramp that confined electrons entering antiparallel to the magnetic field to the side from which they came, the right. This resulted in a relative excess of electron moving parallel to the magnetic field at the left side and a resulting parallel electron flow. At the same time, when electrons entering from the left passed through the current sheet center, they were accelerated by the electric field, resulting in a larger electron flow to the right of the current sheet center, hence the bifurcation. For MMS3-4, these two regions were merged (cf. Figures 5d and 5e to 5g and 5h).

5. Summary and Conclusions

In this paper we report observations of an electron-scale current sheet embedded in a broader (several ion scales) magnetopause current layer. The current sheet has a finite guide field, bifurcated structure and shows signatures of ongoing magnetic reconnection. Among these signatures are strong out-of-plane currents, Hall currents and the associated Hall magnetic field, and a finite magnetic field normal to the current sheet, indicating magnetic connectivity between the two sides of the current sheet. The perpendicular currents are associated with nongyrotropic electron distributions formed through finite gyroradius effects.

The electron distributions show evidence of pitch angle scattering and acceleration consistent with ongoing magnetic reconnection. By performing test particle simulations in a 1-D current sheet where the model magnetic field is based on the observed field, and the electric field is based on the expected field, we find the following results:

1. The electrons entering from the side of the largest magnetic field curvature are scattered to perpendicular pitch angles and constitute the heated population in the center of the current sheet. Electrons entering from the side of the least curvature can stay close to field aligned throughout the current sheet before they are scattered and simultaneously ejected at the opposite side.
2. The modeled electric field shifted the test particle electrons in the center of the current sheet toward parallel pitch angles $\theta = 0°$, explaining an observed electron depletion at pitch angles $\theta = 180°$. The direction of the modeled electric field is consistent with the direction and magnitude of the reconnection electric

field in this magnetic topology. We therefore suggest that an out-of-plane electric field, consistent with the reconnection electric field, is required to explain the observed electron distributions.

Since the reconnecting current sheet was not located directly at the magnetopause but was embedded into the magnetopause boundary layer, we do not expect it to be directly related to the large-scale energy conversion associated with magnetopause reconnection. On the other hand, it is possible that the observed boundary layer itself was formed by such a large-scale magnetopause reconnection event. The role of this electron scale reconnecting current sheet could therefore be to untangle the twisted magnetic fields that could have formed in a large-scale turbulent reconnection exhaust, similar to simulations by Daughton et al. (2011). In the process, this could lead to further acceleration and heating of electrons.

Acknowledgments
We thank the entire MMS team and instrument PIs for data access and support. MMS data are available at https://lasp.colorado.edu/mms/sdc/public. Work at the University of Bergen was supported by the Research Council of Norway/CoE under contract 223252/F50. Work at the Swedish Institute of Space Physics was supported by the Swedish National Space Board, grants 23/12:2 and 128/17. Work at IRAP was supported by CNRS and CNES.

References

Asano, Y., Nakamura, R., Baumjohann, W., Runov, A., Vörös, Z., Volwerk, M., et al. (2005). How typical are atypical current sheets? *Geophysical Research Letters*, *32*, L03108. https://doi.org/10.1029/2004GL021834

Bessho, N., Chen, L.-J., Shuster, J. R., & Wang, S. (2014). Electron distribution functions in the electron diffusion region of magnetic reconnection: Physics behind the fine structures. *Geophysical Research Letters*, *41*, 8688–8695. https://doi.org/10.1002/2014GL062034

Biskamp, D. (2000). Magnetic reconnection in plasmas, *Cambridge monographs on plasma physics* (Vol. 3, pp. 387). Cambridge, UK: Cambridge University Press.

Buechner, J., & Zelenyi, L. M. (1989). Regular and chaotic charged particle motion in magnetotaillike field reversals. I—Basic theory of trapped motion. *Journal of Geophysical Research*, *94*, 11,821–11,842. https://doi.org/10.1029/JA094iA09p11821

Burch, J. L., Moore, T. E., Torbert, R. B., & Giles, B. L. (2015). Magnetospheric Multiscale overview and science objectives. *Space Science Reviews*, *199*, 5–21. https://doi.org/10.1007/s11214-015-0164-9

Burch, J. L., & Phan, T. D. (2016). Magnetic reconnection at the dayside magnetopause: Advances with MMS. *Geophysical Research Letters*, *43*, 8327–8338. https://doi.org/10.1002/2016GL069787

Burch, J. L., Torbert, R. B., Phan, T. D., Chen, L.-J., Moore, T. E., Ergun, R. E., et al. (2016). Electron-scale measurements of magnetic reconnection in space. *Science*, *352*, aaf2939. https://doi.org/10.1126/science.aaf2939

Chen, L.-J., Hesse, M., Wang, S., Bessho, N., & Daughton, W. (2016). Electron energization and structure of the diffusion region during asymmetric reconnection. *Geophysical Research Letters*, *43*, 2405–2412. https://doi.org/10.1002/2016GL068243

Daughton, W., Roytershteyn, V., Karimabadi, H., Yin, L., Albright, B. J., Bergen, B., & Bowers, K. J. (2011). Role of electron physics in the development of turbulent magnetic reconnection in collisionless plasmas. *Nature Physics*, *7*(7), 539–542.

Eastwood, J. P., Phan, T. D., Øieroset, M., & Shay, M. A. (2010). Average properties of the magnetic reconnection ion diffusion region in the Earth's magnetotail: The 2001-2005 Cluster observations and comparison with simulations. *Journal of Geophysical Research*, *115*, A08215. https://doi.org/10.1029/2009JA014962

Egedal, J., Daughton, W., Drake, J. F., Katz, N., & Lê, A. (2009). Formation of a localized acceleration potential during magnetic reconnection with a guide field. *Physics of Plasmas*, *16*(5), 50701. https://doi.org/10.1063/1.3130732

Ergun, R. E., Tucker, S., Westfall, J., Goodrich, K. A., Malaspina, D. M., Summers, D., et al. (2014). The axial double probe and fields signal processing for the MMS mission. *Space Science Reviews*, *199*, 167–188. https://doi.org/10.1007/s11214-014-0115-x

Eriksson, E., Vaivads, A., Graham, D. B., Khotyaintsev, Y. V., Yordanova, E., Hietala, H., et al. (2016). Strong current sheet at a magnetosheath jet: Kinetic structure and electron acceleration. *Journal of Geophysical Research: Space Physics*, *121*, 9608–9618. https://doi.org/10.1002/2016JA023146

Gosling, J. T., & Szabo, A. (2008). Bifurcated current sheets produced by magnetic reconnection in the solar wind. *Journal of Geophysical Research*, *113*, A10103. https://doi.org/10.1029/2008JA013473

Graham, D. B., Khotyaintsev, Y. V., Vaivads, A., Norgren, C., André, M., Webster, J. M., et al. (2017). Instability of agyrotropic electron beams near the electron diffusion region. *Physical Review Letters*, *119*(2), 25101. https://doi.org/10.1103/PhysRevLett.119.025101

Hesse, M., Aunai, N., Sibeck, D., & Birn, J. (2014). On the electron diffusion region in planar, asymmetric, systems. *Geophysical Research Letters*, *41*, 8673–8680. https://doi.org/10.1002/2014GL061586

Hesse, M., Kuznetsova, M., & Birn, J. (2004). The role of electron heat flux in guide-field magnetic reconnection. *Physics of Plasmas*, *11*, 5387–5397. https://doi.org/10.1063/1.1795991

Hesse, M., & Schindler, K. (1988). A theoretical foundation of general magnetic reconnection. *Journal of Geophysical Research*, *93*, 5559–5567. https://doi.org/10.1029/JA093iA06p05559

Hoshino, M., Nishida, A., Mukai, T., Saito, Y., Yamamoto, T., & Kokubun, S. (1996). Structure of plasma sheet in magnetotail: Double-peaked electric current sheet. *Journal of Geophysical Research*, *101*, 24,775–24,786. https://doi.org/10.1029/96JA02313

Lavraud, B., Zhang, Y. C., Vernisse, Y., Gershman, D. J., Dorelli, J., Cassak, P. A., et al. (2016). Currents and associated electron scattering and bouncing near the diffusion region at Earth's magnetopause. *Geophysical Research Letters*, *43*, 3042–3050. https://doi.org/10.1002/2016GL068359

Lindqvist, P.-A., Olsson, G., Torbert, R. B., King, B., Granoff, M., Rau, D., et al. (2014). The spin-plane double probe electric field instrument for MMS. *Space Science Reviews*, *199*, 137–165. https://doi.org/10.1007/s11214-014-0116-9

Liu, Y.-H., Birn, J., Daughton, W., Hesse, M., & Schindler, K. (2014). Onset of reconnection in the near magnetotail: PIC simulations. *Journal of Geophysical Research: Space Physics*, *119*, 9773–9789. https://doi.org/10.1002/2014JA020492

Mozer, F. S., Bale, S. D., & Phan, T. D. (2002). Evidence of diffusion regions at a subsolar magnetopause crossing. *Physical Review Letters*, *89*, 15002. https://doi.org/10.1103/PhysRevLett.89.015002

Nagai, T., Shinohara, I., Fujimoto, M., Hoshino, M., Saito, Y., Machida, S., & Mukai, T. (2001). Geotail observations of the Hall current system: Evidence of magnetic reconnection in the magnetotail. *Journal of Geophysical Research*, *106*, 25,929–25,950. https://doi.org/10.1029/2001JA900038

Norgren, C., Graham, D. B., Khotyaintsev, Y. V., André, M., Vaivads, A., Chen, L.-J., et al. (2016). Finite gyroradius effects in the electron outflow of asymmetric magnetic reconnection. *Geophysical Research Letters*, *43*, 6724–6733. https://doi.org/10.1002/2016GL069205

Øieroset, M., Phan, T. D., Fujimoto, M., Lin, R. P., & Lepping, R. P. (2001). In situ detection of collisionless reconnection in the Earth's magnetotail. *Nature*, *412*, 414–417. https://doi.org/10.1038/35086520

Paschmann, G., Papamastorakis, I., Sckopke, N., Haerendel, G., Sonnerup, B. U. O., Bame, S. J., et al. (1979). Plasma acceleration at the Earth's magnetopause—Evidence for reconnection. *Nature*, *282*, 243–246. https://doi.org/10.1038/282243a0

Phan, T. D., Eastwood, J. P., Cassak, P. A., Øieroset, M., Gosling, J. T., Gershman, D. J., et al. (2016). MMS observations of electron-scale filamentary currents in the reconnection exhaust and near the X line. *Geophysical Research Letters*, *43*, 6060–6069. https://doi.org/10.1002/2016GL069212

Phan, T. D., Eastwood, J. P., Shay, M. A., Drake, J. F., Sonnerup, B. U. Ö., Fujimoto, M., et al. (2018). Electron magnetic reconnection without ion coupling in Earth's turbulent magnetosheath. *Nature*, *557*, 202–206. https://doi.org/10.1038/s41586-018-0091-5

Pollock, C., Moore, T., Jacques, A., Burch, J., Gliese, U., Saito, Y., et al. (2016). Fast plasma investigation for Magnetospheric Multiscale. *Space Science Reviews*, *199*, 331–406. https://doi.org/10.1007/s11214-016-0245-4

Priest, E., & Forbes, T. (2000). *Magnetic reconnection*. Cambridge: Cambridge University Press.

Pritchett, P. L., & Coroniti, F. V. (2004). Three-dimensional collisionless magnetic reconnection in the presence of a guide field. *Journal of Geophysical Research*, *109*, A01220. https://doi.org/10.1029/2003JA009999

Rager, A. C., Dorelli, J. C., Gershman, D. J., Uritsky, V., Avanov, L. A., Torbert, R. B., et al. (2018). Electron crescent distributions as a manifestation of diamagnetic drift in an electron-scale current sheet: Magnetospheric Multiscale observations using new 7.5 ms fast plasma investigation moments. *Geophysical Research Letters*, *45*, 578–584. https://doi.org/10.1002/2017GL076260

Retinò, A., Sundkvist, D., Vaivads, A., Mozer, F., André, M., & Owen, C. J. (2007). In situ evidence of magnetic reconnection in turbulent plasma. *Nature Physics*, *3*, 236–238. https://doi.org/10.1038/nphys574

Runov, A., Nakamura, R., Baumjohann, W., Zhang, T. L., Volwerk, M., Eichelberger, H.-U., & Balogh, A. (2003). Cluster observation of a bifurcated current sheet. *Geophysical Research Letters*, *30*(2), 1036. https://doi.org/10.1029/2002GL016136

Russell, C. T., Anderson, B. J., Baumjohann, W., Bromund, K. R., Dearborn, D., Fischer, D., et al. (2014). The Magnetospheric Multiscale magnetometers. *Space Science Reviews*, *199*, 189–256. https://doi.org/10.1007/s11214-014-0057-3

Schindler, K., & Hesse, M. (2008). Formation of thin bifurcated current sheets by quasisteady compression. *Physics of Plasmas*, *15*(4), 42902. https://doi.org/10.1063/1.2907359

Shay, M. A., Drake, J. F., Rogers, B. N., & Denton, R. E. (2001). Alfvénic collisionless magnetic reconnection and the Hall term. *Journal of Geophysical Research*, *106*, 3759–3772. https://doi.org/10.1029/1999JA001007

Sonnerup, B. U. (1979). Magnetic field reconnection, *Space plasma physics: The study of Solar-System plasmas. Volume 2, Working papers. Part II — Solar System plasma processes* (pp. 879–972). Washington, DC: the National Academy of Sciences.

Sonnerup, B. U. O., Paschmann, G., Papamastorakis, I., Sckopke, N., Haerendel, G., Bame, S. J., et al. (1981). Evidence for magnetic field reconnection at the Earth's magnetopause. *Journal of Geophysical Research*, *86*, 10,049–10,067. https://doi.org/10.1029/JA086iA12p10049

Sundkvist, D., Retinò, A., Vaivads, A., & Bale, S. D. (2007). Dissipation in turbulent plasma due to reconnection in thin current sheets. *Physical Review Letters*, *99*(2), 25004. https://doi.org/10.1103/PhysRevLett.99.025004

Toledo-Redondo, S., André, M., Khotyaintsev, Y. V., Vaivads, A., Walsh, A., Li, W., et al. (2016). Cold ion demagnetization near the X-line of magnetic reconnection. *Geophysical Research Letters*, *43*, 6759–6767. https://doi.org/10.1002/2016GL069877

Vaivads, A., Khotyaintsev, Y., André, M., Retinò, A., Buchert, S. C., Rogers, B. N., et al. (2004). Structure of the magnetic reconnection diffusion region from four-spacecraft observations. *Physical Review Letters*, *93*(10), 105001. https://doi.org/10.1103/PhysRevLett.93.105001

Vasyliunas, V. M. (1972). Nonuniqueness of magnetic field line motion. *Journal of Geophysical Research*, *77*, 6271. https://doi.org/10.1029/JA077i031p06271

Wang, R., Lu, Q., Nakamura, R., Baumjohann, W., Huang, C., Russell, C. T., et al. (2018). An electron-scale current sheet without bursty reconnection signatures observed in the near-Earth tail. *Geophysical Research Letters*, *45*, 4542–4549. https://doi.org/10.1002/2017GL076330

Wilder, F. D., Ergun, R. E., Eriksson, S., Phan, T. D., Burch, J. L., Ahmadi, N., et al. (2017). Multipoint measurements of the electron jet of symmetric magnetic reconnection with a moderate guide field. *Physical Review Letters*, *118*(26), 265101. https://doi.org/10.1103/PhysRevLett.118.265101

Wygant, J. R., Cattell, C. A., Lysak, R., Song, Y., Dombeck, J., McFadden, J., et al. (2005). Cluster observations of an intense normal component of the electric field at a thin reconnecting current sheet in the tail and its role in the shock-like acceleration of the ion fluid into the separatrix region. *Journal of Geophysical Research*, *110*, A09206. https://doi.org/10.1029/2004JA010708

Yau, A. W., & André, M. (1997). Sources of ion outflow in the high latitude ionosphere. *Space Science Reviews*, *80*, 1–25. https://doi.org/10.1023/A:1004947203046

Zenitani, S., Hasegawa, H., & Nagai, T. (2017). Electron dynamics surrounding the X line in asymmetric magnetic reconnection. *Journal of Geophysical Research: Space Physics*, *122*, 7396–7413. https://doi.org/10.1002/2017JA023969

Zenitani, S., & Nagai, T. (2016). Particle dynamics in the electron current layer in collisionless magnetic reconnection. *Physics of Plasmas*, *23*(10), 102102. https://doi.org/10.1063/1.4963008